



Title	Evaluation of Porosity and Its Variation in Porous Materials Using Microfocus X-ray Computed Tomography Considering the Partial Volume Effect
Author(s)	Kato, Masaji; Takahashi, Manabu; Kawasaki, Satoru; Mukunoki, Toshifumi; Kaneko, Katsuhiko
Citation	MATERIALS TRANSACTIONS, 54(9), 1678-1685 https://doi.org/10.2320/matertrans.M-M2013813
Issue Date	2013
Doc URL	http://hdl.handle.net/2115/56962
Type	article
File Information	MT,54(9)2013,1678-1685.pdf



[Instructions for use](#)

Evaluation of Porosity and Its Variation in Porous Materials Using Microfocus X-ray Computed Tomography Considering the Partial Volume Effect

Masaji Kato^{1,*}, Manabu Takahashi², Satoru Kawasaki¹, Toshifumi Mukunoki³ and Katsuhiko Kaneko¹

¹Faculty of Engineering, Hokkaido University, Sapporo 060-8628, Japan

²Institute for Geology and Geoinformation, National Institute of Advanced Industrial Science and Technology (AIST), Tsukuba 305-8567, Japan

³Kumamoto University, Kumamoto 860-8555, Japan

The physical properties of two-phase materials depend on their internal structure. Therefore, segmentation of the structure of such materials is important in material sciences. In this study, we used a maximum likelihood thresholding method that considered the partial volume effect—i.e., the effect of mixels (mixed pixels)—to calculate the porosities of packed glass beads and the Berea sandstone using microfocus X-ray computed tomography (CT) images. We also examined the effects of scanning conditions on the segmentation results and assessed the porosity of possible packing structures of the glass beads to be segmented to be 33–37% based on histogram data. Moreover, we evaluated the porosity of the Berea sandstone to be 18%.

Then, we examined variation in the porosity of biogrouded packing of glass beads using a microfocus X-ray CT scanner and histogram-based image analysis with the same thresholding method. Our results indicated that the ratio of grouted to ungrouted geomaterial porosities was 0.98, whereas the value estimated by measuring changes in the concentration of calcium ions was 0.98–0.99. Thus, we have confirmed that the proposed method can evaluate small changes in porosity with high accuracy. [[doi:10.2320/matertrans.M-M2013813](https://doi.org/10.2320/matertrans.M-M2013813)]

(Received March 18, 2013; Accepted June 13, 2013; Published July 26, 2013)

Keywords: porous material, X-ray CT, partial volume effect, image segmentation, histogram-based thresholding, mixel, maximum likelihood criteria, sandstone, packed glass beads

1. Introduction

Porosity, defined as the ratio of pore volume to the total volume of a porous solid, is a physical property of porous materials and plays an important role in their mechanical and hydraulic behaviour. Therefore, porosity can be an indicator of the mechanical and hydraulic properties of porous materials.

Various approaches have been suggested to measure the porosity of porous materials, including mercury intrusion, nitrogen gas adsorption porosimetry and comparison of the weight of materials under dry and water-saturated conditions.¹⁾ In addition, the pore space of materials can be observed under a microscope in thin section.²⁾ Such methods inevitably involve the destruction of the samples, since they must be cut, polished, heated, or immersed in fluid at the very least; the effects of related disturbances on the samples cannot be ignored.

In this study, we used X-ray computed tomography (CT), a nondestructive technique, to observe and analyse the internal structure of samples and estimate the porosity of porous materials. Many established procedures exist for porosity estimation using X-ray CT. For example, Withjack³⁾ developed a method of calculating porosity using linear attenuation coefficients obtained by sequential scanning of porous material saturated by two kinds of fluids with different density. Van Geet *et al.*⁴⁾ introduced two methods of porosity measurement: a calibration method using a pure nonporous sample for homogeneous monomineralic samples (limestone), and a dual energy technique for heterogeneous samples (sandstone). Their results indicated that porosity

varies slice by slice, typically within a given range. Although this variation depends on the heterogeneity of the rock samples used, the results seem to suggest that the thresholds used in image segmentation affect the porosity obtained.

Here, we present an automatic image segmentation technique for CT images of porous materials that considers the partial volume effect. Then, we discuss the applicability of our technique for the evaluation of porosity and its variation in artificial and natural porous materials.

2. Microfocus X-ray CT

X-ray CT is a nondestructive and noninvasive three-dimensional (3D) visualisation and quantification tool. Microfocus X-ray CT is based on recording X-ray projections of an object at different angles and stacking several sequential slices. A filtered back-projection algorithm is then used to reconstruct a slice image through the object to reveal the distribution of the linear attenuation coefficient. The attenuation coefficient depends on the applied X-ray energy and the atomic number and density of the object. Further descriptions of microfocus X-ray CT instruments and reconstruction algorithms have been presented by Kak and Slaney.⁵⁾

In the present study, we used a microfocus X-ray CT scanner (TOSCANER 31300 µhd, Toshiba IT & Control Systems Co.) installed at Hokkaido University, Japan. This scanner has been used in several previous studies.^{6–9)} The focal spot size of the X-ray source assembly is 5 µm. Scans were conducted at 130 kV (the maximum tube voltage of the device) and 62 µA, and we selected the full-scan mode of a single slice for further study. It is possible to set the number of views (≤ 4800) and number of stacks per angle (≤ 50)

*Corresponding author, E-mail: kato@geo-er.eng.hokudai.ac.jp

arbitrarily. The distance between the focal spot of the X-ray source and the centre of rotation (focus–centre distance; FCD) is also variable (≤ 50 cm) and can be used to vary the resolution of the CT images.

Each square in a two-dimensional image matrix is known as a pixel, and a cubic volumetric pixel in three dimensions is typically known as a voxel. In this study, we used a tiny elongated voxel with cross-sectional dimensions of $5\ \mu\text{m} \times 5\ \mu\text{m}$ and voxel height of approximately $20\ \mu\text{m}$ depending on the FCD; we set the matrix size to be 2048×2048 pixels.

The gain and position of the rotational centre of the CT scanner was carefully calibrated in order to reduce artifacts and obtain clear images. However, some remaining blurriness is inevitable in X-ray CT images. Such blurring is primarily a result of two factors: the penumbra effect, which depends on the focal spot size and the distances between the X-ray source, the object and the detector;¹⁰⁾ and the partial volume effect, which results from the existence of multiple substances in each voxel in the CT images.¹¹⁾ The blur from these effects can be minimised by reducing the focal spot size whilst enhancing the spatial resolution (which is equivalent to minimising voxel size), although the blur cannot be removed completely. In the present study, we modelled the partial volume effect stochastically and then used the resulting model directly in image segmentation.

3. Image Segmentation

3.1 Mixel model

The partial volume effect is a persistent problem in digital images of multiphase materials. To tackle this issue, Choi *et al.*¹²⁾ introduced the concept of the mixel, or mixed pixel, to the classification of medical magnetic resonance images of brains. A mixel contains multiple constituents within a single pixel and blurs the image to some extent. Conversely, pixels with only a single phase are known as pure pixels. Numerous studies have focused on dealing with partial volume effects and/or mixels in medical science,^{13–15)} remote sensing,^{16,17)} soil and rock engineering,¹⁸⁾ and information technology.^{19–22)}

The spatial distribution data of X-ray attenuation coefficients for two-phase materials are typically obtained by X-ray CT scanning. Greyscale images converted from the attenuation coefficient data are obtained as a mixture of pure pixels and mixels (Fig. 1). In fact, the distribution of pure pixels follows a normal distribution. The probability density function (PDF) of class i (corresponding to phase i) within pure pixels can be expressed as follows:

$$f_i(x) = N(x; \mu_i, \sigma_i^2) = \frac{1}{\sqrt{2\pi\sigma_i^2}} \exp\left\{-\frac{(x - \mu_i)^2}{2\sigma_i^2}\right\} \quad (i = 1, 2) \quad (1)$$

where $N(x; \mu_i, \sigma_i^2)$ denotes the normal distribution function for intensity level x , expectation μ_i and variance σ_i^2 of class i . For mixels, the area proportion distribution is assumed to be an extension of the beta distribution, and the PDF of mixels is given by the following equation:²⁰⁾

$$M(x) = \frac{1}{B(m, n)} \int_0^1 a^{m-1} (1-a)^{n-1} N(x; \mu_a, \sigma_a^2) da \quad (2)$$

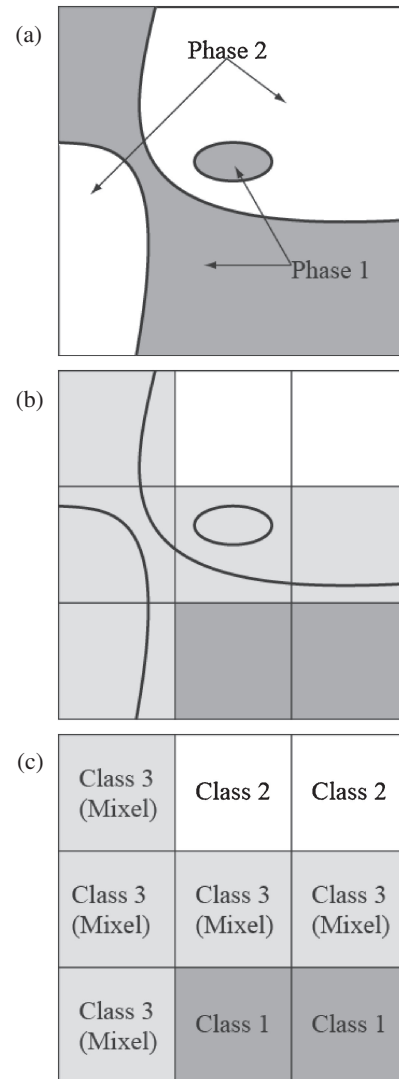


Fig. 1 Schematic of image acquisition. Three-class images are constructed from two-phase material by quantisation: (a) a real image, (b) its quantised image with partial volume effect, and (c) the obtained three-class digital image.

where the beta function is $B(m, n) = \int_0^1 a^{m-1} (1-a)^{n-1} da$. a is the area proportion of constituent class 1 and $1-a$ is that of constituent class 2 ($0 \leq a \leq 1$); parameters m and n are greater than 0, and μ_a and σ_a^2 are as follows:

$$\mu_a = a\mu_1 + (1-a)\mu_2 \quad (3)$$

$$\sigma_a^2 = a^2\sigma_1^2 + (1-a)^2\sigma_2^2 \quad (4)$$

For simplicity, we set the parameters m and n in the beta function to 1 in the present study, based on the assumption that the boundary between the two phases of a material is simple and smooth. We assigned mixels to class 3. An example of the distribution of two-class mixels is shown in Fig. 2, in which the intensity-level histogram represents the superposition of the normal distributions for pure pixels and mixel distribution using a beta function for mixed pixels.

3.2 Thresholding method

Numerous thresholding techniques have been described in the literature.^{23–25)} However, the performance of each technique depends on its specific purpose and the object of

Table 1 Maximum likelihood thresholding criteria corresponding to statistics of each class (modified from Sekita *et al.*³⁰); M is the total number of classes, \mathbf{t} is the threshold vector where the number of vector elements equals $M - 1$, $\tilde{\omega}_k$ and $\tilde{\sigma}_k^2$ are the occurrence probability and variance, respectively, of class k and $\tilde{\sigma}^2$ denotes the expectation of variance within each class.

		Variance of each class, σ_k^2	
		Nearly equal	Different
Occurrence probability of each class, ω_k	Nearly equal	$J_O(\mathbf{t}) = -\ln \tilde{\sigma}$ (Otsu ³¹)	$J_D(\mathbf{t}) = -\sum_{k=1}^M \tilde{\omega}_k \ln \tilde{\sigma}_k$ (Sekita <i>et al.</i> ³⁰)
	Different	$J_Q(\mathbf{t}) = \sum_{k=1}^M \tilde{\omega}_k \ln \frac{\tilde{\omega}_k}{\tilde{\sigma}}$ (Kurita <i>et al.</i> ³²)	$J_K(\mathbf{t}) = \sum_{k=1}^M \tilde{\omega}_k \ln \frac{\tilde{\omega}_k}{\tilde{\sigma}_k}$ (Kittler and Illingworth ³³)

analysis. Baveye *et al.*²⁶ reported difficulty in applying thresholding to photographs and X-ray CT images of soils and the dependence of the outcome on the observer. Iassonov *et al.*²⁷ presented an overview of thresholding techniques applied in recent porous media research. Kitamoto^{28,29} demonstrated the application of a mixel model to image classification of satellite images, allowing separation of the cloud phase from the sea phase.

Here, we limited the scope of the investigation to two-phase segmentation problems with a bimodal histogram obtained from digital images. The applicability of this method to the images was checked using a segmentation index,⁹ which quantifies the extent to which a histogram exhibits a sharp bimodal distribution. We also adopted the maximum likelihood thresholding method proposed by Kitamoto,²⁸ which considers the effect of mixels, for two-phase segmentation problems. Accordingly, the total number of classes M was three (two for pure pixels and one for mixels), and two thresholds were employed: one between classes 1 and 3, and another between classes 2 and 3. These thresholds are referred to as t_1 and t_2 , respectively, and can be expressed by the vector $\mathbf{t} = (t_1, t_2)$.

The maximum likelihood thresholding criteria used in the present study ($J_O(\mathbf{t})$, $J_D(\mathbf{t})$, $J_Q(\mathbf{t})$ and $J_K(\mathbf{t})$) are functions of the threshold vector \mathbf{t} and are presented in Table 1 (modified from Sekita *et al.*³⁰) with the corresponding statistical properties of each class. The expectation of variance within each class $\tilde{\sigma}^2$ used in the table is expressed as follows:

$$\tilde{\sigma}^2 = \sum_{k=1}^M \tilde{\omega}_k \tilde{\sigma}_k^2 \quad (5)$$

Because $\tilde{\sigma}^2$ is calculated using the occurrence probability $\tilde{\omega}_k$ and variance $\tilde{\sigma}_k^2$ of class k , all maximum likelihood thresholding criteria presented in Table 1 were decided using both $\tilde{\omega}_k$ and $\tilde{\sigma}_k^2$.

After obtaining histogram data from the images, the threshold vector \mathbf{t} was selected according to the following steps.

(1) Check whether the histogram exhibits a bimodal distribution geometrically.

(2) Set the intensity levels to x_{p1} and x_{p2} at the left and right peaks (where $x_{p1} < x_{p2}$), respectively, and to x_v for the trough between the two peaks of the histogram temporarily.

(3) Given the threshold vector $\mathbf{t} = (t_1, t_2)$, calculate the expectations and variances of classes 1 and 2 for pure pixels from the histogram data. Then, using these values, estimate the stochastic parameters of class 3 for mixels analytically using eqs. (2)–(4). Accordingly, determine the threshold vector \mathbf{t} in the possible range to maximise the likelihood

given in Table 1; t_1 and t_2 should be between x_{p1} and x_v and between x_v and x_{p2} , respectively.

We automated the procedure above for the selection of threshold values. The expectations and variances of classes 1 and 2 in the digital images were unknown prior to thresholding. Accordingly, $J_K(\mathbf{t})$ was selected as the first thresholding criterion. However, thresholding in this manner sometimes resulted in both thresholds being almost equal. In such cases, we applied another criterion, $J_D(\mathbf{t})$.

3.3 Porosity calculation

The porosity can be evaluated once the thresholds are set. We refer to the frequencies of pixels within classes 1, 2 and 3 as N_1 , N_2 and N_3 , respectively. Here, class 1 refers to the pixels to the left of threshold t_1 in the image histogram, class 2 to those to the right of threshold t_2 , and class 3 to those between the thresholds t_1 and t_2 . Using this method, we were able to obtain the ratio of the occurrence probability of all three classes (two classes for pure pixels and one class for mixels). However, the area (volume) of mixels must eventually be divided into two phases in order to evaluate porosity. It is reasonable to assume that the area of mixels can be divided into two phases according to the ratio between the numbers of pixels in classes 1 and 2.^{8,34} Thus, the porosity of porous material ϕ can be calculated according to the following equation:

$$\phi = \frac{N_1 + N_3 \frac{N_1}{N_1 + N_2}}{N} = \frac{N_1}{N_1 + N_2} \quad (6)$$

where N_1 , N_2 and N_3 are the numbers of pixels within classes 1, 2 and 3, respectively, and N is the total number of pixels (i.e., is equivalent to the sum of N_1 , N_2 and N_3). Note that the number of mixels (i.e., pixels in class 3) does not appear in the final calculation of the porosity.

4. Porosity Measurements

4.1 Porosity of packing of glass beads

We applied the thresholding method described above to X-ray CT images of glass bead packing and evaluated the porosity. We also examined the effects of scanning conditions on the segmentation results.

Glass beads with a mean density of 2500 kg/m³ and mean particle diameter of 0.38 mm were gently placed into a polystyrene bottle with a diameter of 21.0 mm and height of 54.8 mm. We scanned this specimen using a microfocus X-ray CT scanner under various conditions, varying the number of views (500–4800), number of stacks per angle (10–50) and

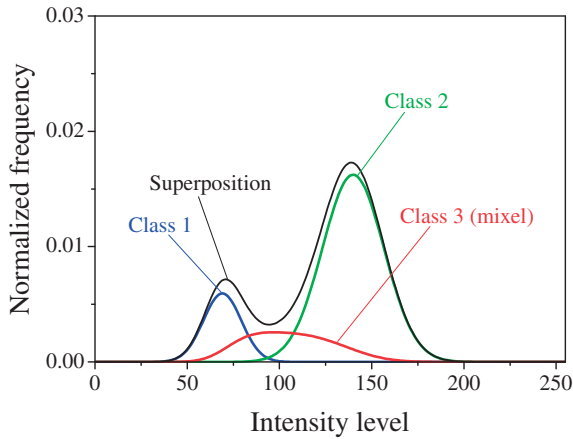


Fig. 2 Example of two-class mixel distribution. Lines show probability distributions of three classes and their superposition.

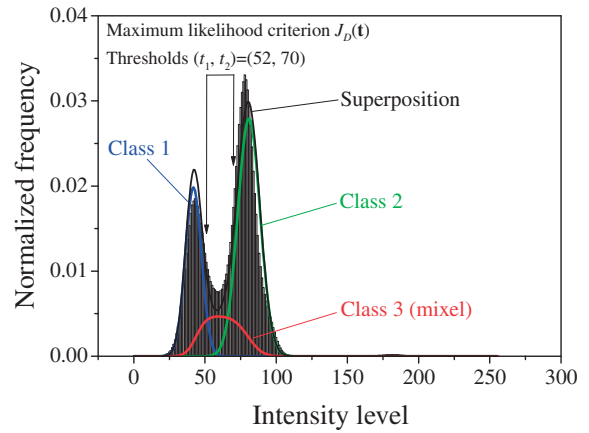
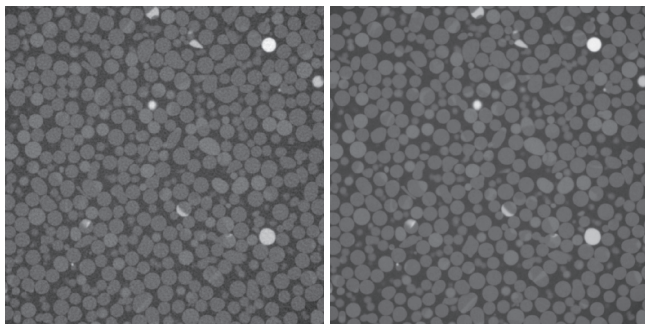


Fig. 4 Histogram of greyscale CT image of packed glass beads in Fig. 3(a). Lines show probability distributions of three classes and their superposition. Selected thresholds are shown in this figure.



(a) 500 views and 50 stacks (b) 4800 views and 50 stacks

Fig. 3 CT image of packed glass beads with mean particle diameter of 0.38 mm, obtained under different numbers of views and the same stack number. Bright region represents a high-attenuation substance (i.e., glass beads in the specimen), while the dark region represents a low-attenuation substance (i.e., voids in the specimen).

Table 2 Estimated porosity of packed glass beads corresponding to FCDs.

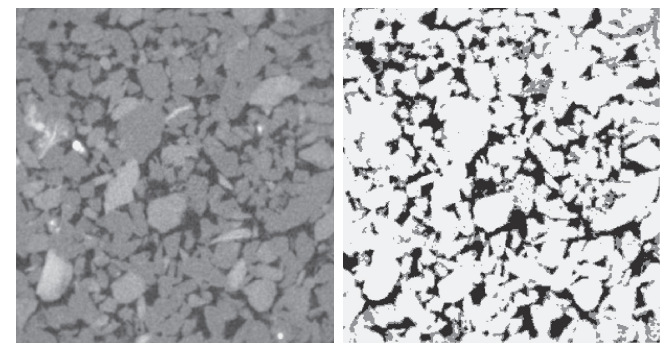
FCD (mm)	140	160	180	200	205	210	220
Porosity (%)	33.3	34.2	35.6	35.1	35.0	36.7	36.1

FCD (100–260 mm). A greyscale image converted from the X-ray attenuation coefficient is illustrated in Fig. 3. The bright region represents the presence of a high-attenuation substance (i.e., glass beads in the specimen), whereas the dark region represents that of a low-attenuation substance (i.e., voids in the specimen). Several glass particles were white in colour owing to the heterogeneous glass bead density. Histograms of the greyscale images are presented in Fig. 4, which includes lines indicating the probability distributions of the three classes. The superposition of these probability distributions corresponds to the histogram of the image. Typically, high-density data must be removed from the histogram before image analysis. However, the frequency of high-density data (i.e., white areas in the image) was not particularly high in the present study.

We evaluated the porosities of the specimen under different conditions using the porosity calculation equation described above; the relationship between the porosity of the glass beads and FCD (i.e., when all other scanning conditions were held constant) is presented in Table 2.

4.2 Porosity of sandstone

We applied the same thresholding method to the X-ray CT images of the Berea sandstone to evaluate its porosity. The



(a) Original image (b) Segmented image

Fig. 5 (a) Original X-ray CT image of the Berea sandstone (size 3.54 mm × 3.34 mm); bright region represents a high-attenuation substance (i.e., mineral in the specimen) and the dark region represents a low-attenuation substance (i.e., pores in the specimen). (b) Image segmented using thresholding method based on mixel model ($t_1 = 87$ and $t_2 = 118$); black regions represent class 1 (pores), white regions represent class 2 (minerals) and grey regions represent class 3 (mixels).

Berea sandstone has been used in many previous investigations relating to rock mechanics, producing substantial scientific datasets.^{35–40}

A greyscale X-ray CT image of the Berea sandstone is shown in Fig. 5. As in Fig. 3, the bright region represents a high-attenuation substance (i.e., mineral in the specimen), and the dark region represents a low-attenuation substance (i.e., pores in the specimen). The histogram of the CT images is shown in Fig. 6 and indicates that the distance between the means of two classes is relatively small; this may lead to errors in the thresholded images. The logarithmic likelihood distributions corresponding to threshold vector \mathbf{t} are presented in Fig. 7. The criterion $J_D(\mathbf{t})$ (Fig. 7(a)) was adopted instead of $J_K(\mathbf{t})$, and the threshold vector \mathbf{t} was determined at the point of maximum $J_D(\mathbf{t})$. We found the criterion of $J_K(\mathbf{t})$

Table 3 Porosities of the Berea sandstone obtained by different methods.

Method	Porosity (%)
This study	18.4 (–23.7)
Mercury intrusion porosimetry	19.4–22.7
Reference ⁴¹⁾	16.2, 19.0

(Fig. 7(b)) to be unsuitable because both thresholds were nearly equal at the point of maximum $J_K(\mathbf{t})$. The frequencies of all three classes obtained from the histogram-based analysis are illustrated in Fig. 6.

We determined the porosity of this sandstone—evaluated using eq. (6) with area occupancies of 0.153 in class 1 (pores), 0.679 in class 2 (minerals) and 0.168 in class 3 (mixel)—to be 18.4%. For reference, the porosity will be 23.7% if pores represent half of the total mixel area. These values of porosity are presented in Table 3, with the latter value in parentheses.

4.3 Estimation of porosity variation

In the previous sections, we described our evaluation of the porosities of porous materials. Here, we focus on variations in porosity within a porous material. Takahashi *et al.*⁴⁰⁾ quantified changes in the pore geometry of the Berea sandstone based on increases in hydrostatic pressure. In this study, we considered the following materials: sands, glass beads, gum tips, plastic pellets, and steel balls. However, we opted to study the packing of glass beads owing to the relative ease of measuring porosity for this material.

The porosity of the glass beads was altered artificially using a biogrouting technique.⁴²⁾ The specimens were prepared by mixing a grout solution for glass beads in a polystyrene bottle (Table 4); the glass beads and polystyrene bottle are the same as those described in Section 4.1. Although the use of the same specimen for both the grouted and ungrouted conditions is desirable, we used two different specimens to prevent yeast from being exterminated during the first X-ray irradiation of the ungrouted specimen. To test the grouted condition, we prepared the specimen by mixing it with yeast and leaving it to rest for 24 h in an incubator at 25°C. In contrast, the ungrouted specimen was mixed without yeast.

The specimens were scanned using the CT scanner in the single-slice mode; the resolution (voxel size) of the CT images was $5\ \mu\text{m} \times 5\ \mu\text{m} \times 16\ \mu\text{m}$. We imaged 12 slices from each specimen to enhance the reliability. Examples of X-ray images of the grouted and ungrouted specimens are presented in Fig. 8. The white to light grey regions represent glass beads, whereas the black to dark grey regions represent the solution. Figure 9 illustrates the histograms of average X-ray attenuation coefficient determined from the 12 measured slices. The bell-shaped distribution on the left of each plot corresponds to the dark region (i.e., the solution), while that on the right corresponds to the bright region (i.e., glass beads).

We assigned pure pixels of the solution (dark grey) to class 1, pure pixels of glass beads (light grey) to class 2, and mixels to class 3. The area occupied by each class was calculated by integrating the frequency of each class using

Table 4 Constituents of grout solution.

1 M Tris-HCl	100 (mL)
Glucose	3.0 (g)
Calcium nitrate tetrahydrate	23.6 (g)

Table 5 Area occupancies of three classes and porosities of grouted and ungrouted packed glass beads.

	Area occupancy (%)			Porosity (%)
	Class 1 (liquid phase)	Class 2 (solid phase)	Class 3 (mixed phase)	
Ungrouted	29.5	55.1	15.4	34.9
Grouted	28.8	55.7	15.5	34.0

the estimated thresholds (Table 5). Then, we calculated the porosity by substituting the calculated areas in eq. (6). Moreover, we calculated the average porosities of 12 slices of each of the grouted and ungrouted specimens (Table 5). The ratio of the average porosity of the grouted specimen to that of the ungrouted specimen was 0.98.

5. Discussion

The average porosity of the packed glass beads that were gently placed in a bottle was 33.3–36.7% (Table 2); this range corresponds to porosity values lying somewhere between the tetragonal sphenoidal and cubical tetrahedral packing systems.⁴³⁾ This is a reasonable result considering the glass bead packing process.

Our method obtained a porosity of 18.4% for the Berea sandstone. The porosity of 23.7%, calculated based on the assumption that pores represent half of the total mixel area, seems to be an overestimation. Accordingly, this value is given in parentheses in Table 3. We also measured the porosity of Berea sandstone, which was sampled from the same block used in this study, using mercury intrusion porosimetry. Some general values of the porosity of the same rock were presented in a previous study.⁴¹⁾ Our results obtained from the image analysis are in good agreement with porosity values measured by other methods (see Table 3).

We compared the results obtained using our method with those obtained using two simple conventional methods of automatic image segmentation (Fig. 10): median thresholding and the maximum entropy method.⁴⁴⁾ When applying median thresholding, the ratio of the domain above and below the selected threshold becomes 50% in any image, indicating that the porosity is also 50%. This does not necessarily mean that median thresholding is applicable to porosity evaluation. In the meantime, the maximum entropy method sets a threshold based on the maximum entropy principle. Maximum entropy criterion 2 exhibits relatively good results in this particular instance in Fig. 10, although the technique may not always produce such positive results. Our results suggest that the occurrence of a peak of information entropy towards an edge of the histogram or the occurrence of a double peak may be inappropriate.

Shoji⁴⁵⁾ estimated the ratio of the porosity of a biogrouted specimen to that of an ungrouted specimen by measuring the

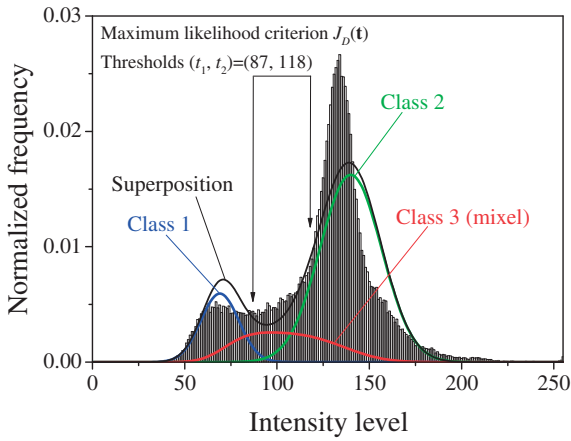
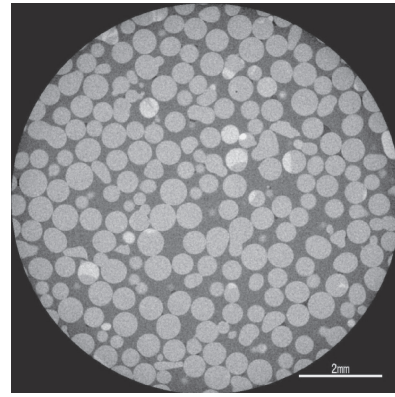
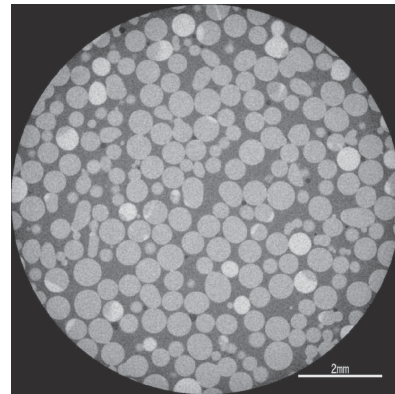


Fig. 6 Histogram of image in Fig. 5(a). Lines show probability distributions of three classes and their superposition. Selected thresholds (see Fig. 7) are shown in this figure.



(a) UngROUTED



(b) Grouted

Fig. 8 X-ray CT images of (a) ungrouted and (b) grouted packed glass beads. White to light grey regions represent glass beads, while black to dark grey regions represent the solution.

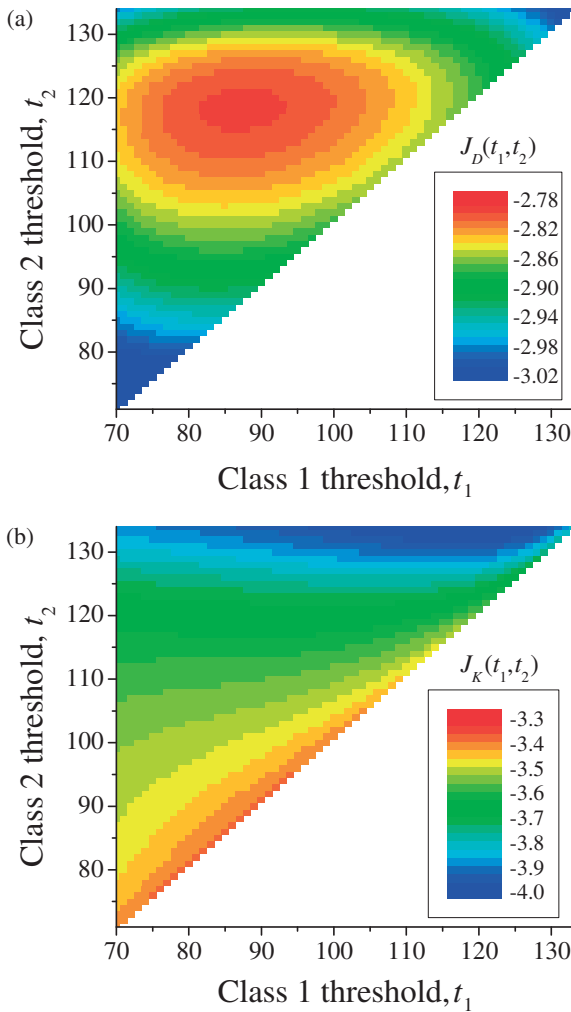


Fig. 7 Logarithmic likelihood distributions corresponding to threshold vector \mathbf{t} : (a) $J_D(\mathbf{t})$ and (b) $J_K(\mathbf{t})$. From (a), threshold vector \mathbf{t} is determined at maximum $J_D(\mathbf{t})$ point as follows: $t_1 = 87$ and $t_2 = 118$. In (b), because both thresholds are nearly equal, this criterion is not suitable.

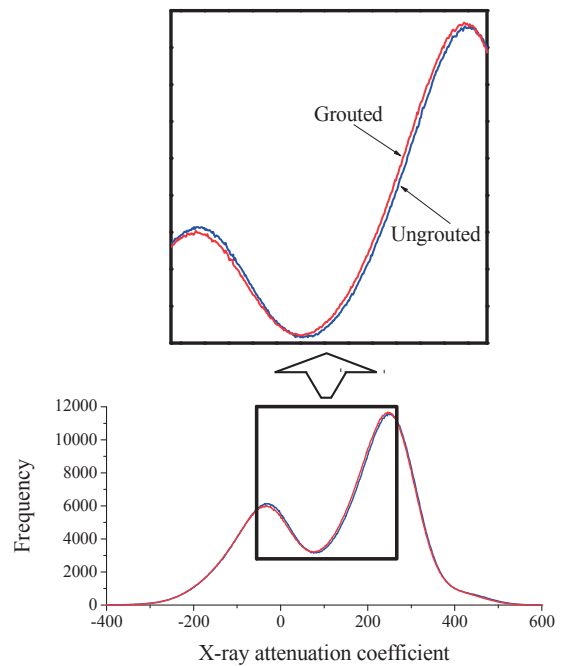


Fig. 9 Distributions of X-ray attenuation coefficients for ungrouted and grouted packed glass beads in Fig. 8. The bell-shaped distribution on the left of each plot corresponds to the dark region (i.e., the solution), while that on the right corresponds to the bright region (i.e., glass beads).

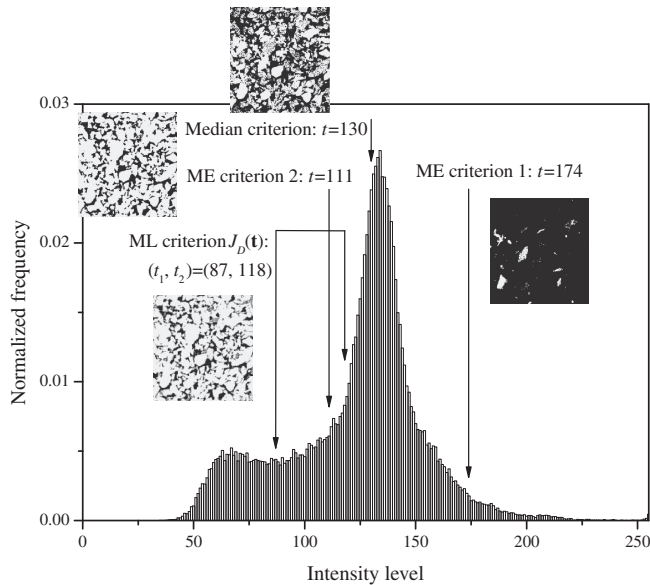


Fig. 10 Comparison of selected thresholds and segmented images obtained by each method. Segmented images correspond to Fig. 5 but reduced in size. ME: maximum entropy; ML: maximum likelihood.

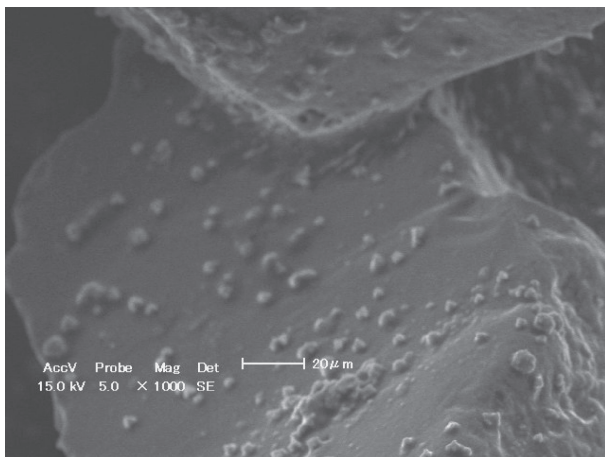


Fig. 11 SEM image of grouted sands. Calcium carbonate deposited on surface of sand grains and between grains.⁴⁶⁾

concentration of calcium ions and found this ratio to be 0.98–0.99. This can be explained by the deposition of calcium carbonate on the surface of particles in the grouted specimen. Figure 11 provides evidence for the deposition of calcium carbonate on the grain surfaces and between the grains in the grouted sands. The porosity derived as described in Section 4.3 is in good agreement with that presented by Shoji.⁴⁵⁾ Thus, our method employing X-ray CT and the maximum likelihood thresholding method considering the effects of mixels enables us to evaluate changes in porosity with high accuracy. This method makes it possible to evaluate a diverse range of changes in porosity from one percent to several tens of percent.

6. Conclusions

In the present study, we introduced a thresholding method that considers the partial volume effect and applied this method to calculate the porosity of packed glass beads using

X-ray CT images. Furthermore, we examined the effects of scanning conditions on the segmentation results and applied our thresholding method successfully in a calculation of the porosity of the Berea sandstone using X-ray CT images.

In order to focus on variations in porosity within the same porous materials, we measured biogrouted and ungrouted packing of glass beads using X-ray CT and evaluated their respective porosities using the thresholding method. Our results show that this novel method allows the evaluation of small changes in porosity with high accuracy.

Appendix

$f_i(x)$ probability density function of class i within pure pixels

$N(x; \mu_i, \sigma_i^2)$ normal distribution function

x intensity level

μ_i expectation of class i

σ_i^2 variance of class i

$M(x)$ probability density function of mixels

$B(m, n)$ beta function

a the area proportion of constituent class 1 ($0 \leq a \leq 1$)

μ_a expectation of mixel class

σ_a^2 variance of mixel class

$J_O(t)$, $J_D(t)$, $J_Q(t)$, $J_K(t)$: maximum likelihood thresholding criteria

M the total number of classes

\mathbf{t} threshold vector where the number of vector elements equals $M - 1$

x_{p1} intensity level at left peak of bimodal histogram

x_{p2} intensity level at right peak of bimodal histogram

x_v intensity level at trough between two peaks of bimodal histogram

$\tilde{\omega}_k$ occurrence probability of class k

$\tilde{\sigma}_k^2$ variance of class k

$\tilde{\sigma}^2$ expectation of variance within each class

N_1 the number of pixels within class 1

N_2 the number of pixels within class 2

N_3 the number of pixels within class 3 (mixel class)

N the total number of pixels (the sum of N_1 , N_2 and N_3)

ϕ porosity of porous material

Acknowledgements

Some of the X-ray CT images were obtained by Messrs Y. Kobayashi and H. Yamanaka from Hokkaido University (HU). Dr. D. Fukuda from HU gave us valuable comments. We thank them for their contributions. Part of this research was supported by a Grant-in-Aid for Scientific Research (b) from the Ministry of Education, Culture, Sports, Science and Technology (No. 21300326).

REFERENCES

- 1) R. Denoyel and M. Thommes (Eds.): Part. Part. Syst. Charact. (Special Issue) **23** (2006).
- 2) A. B. Abell, K. L. Willis and D. A. Lange: *J. Colloid Interf. Sci.* **211** (1999) 39–44.
- 3) E. M. Withjack: *SPE Form. Eval.* **3** (1988) 696–704.
- 4) M. Van Geet, D. Lagrou and R. Swennen: *Applications of X-ray Computed Tomography in the Geosciences*, ed. by F. Mees, R.

- Swennen, M. Van Geet and P. Jacobs, Vol. 215, (Geological Society, London, 2003) pp. 51–60.
- 5) A. C. Kak and M. Slaney: *Principles of Computerized Tomographic Imaging*, (SIAM, New York, 1988) p. 327.
 - 6) M. Kato, Y. Kobayashi, S. Kawasaki and K. Kaneko: *Geoinformatics* **20** (2009) 112–113 (in Japanese).
 - 7) C. Kawaragi, T. Yoneda, T. Sato and K. Kaneko: *Eng. Geology* **106** (2009) 51–57.
 - 8) Y. Kobayashi, S. Kawasaki, M. Kato, T. Mukunoki and K. Kaneko: *J. MMIJ* **125** (2009) 540–546 (in Japanese).
 - 9) H. Yamanaka, S. Kawasaki, M. Kato, T. Mukunoki and K. Kaneko: *Jpn. Geotechnical J.* **6** (2011) 273–284 (in Japanese).
 - 10) T. S. Curry III, J. E. Dowdey and R. C. Murry, Jr.: *Christensen's Physics of Diagnostic Radiology*, 4th edn., (Lea & Febiger, Philadelphia, London, 1990) p. 522.
 - 11) R. A. Ketcham and W. D. Carlson: *Comput. Geosci.* **27** (2001) 381–400.
 - 12) H. S. Choi, D. R. Haynor and Y. M. Kim: *IEEE Trans. Med. Imag.* **10** (1991) 395–407.
 - 13) D. W. Shattuck, S. R. Sandor-Leahy, K. A. Schaper, D. A. Rottenberg and R. M. Leahy: *NeuroImage* **13** (2001) 856–876.
 - 14) J. Tohka, A. Zijdenbos and A. Evans: *NeuroImage* **23** (2004) 84–97.
 - 15) J. S. Kim, V. Singh, J. K. Lee, J. Lerch, Y. Ad-Dab'bagh, D. MacDonald, M. L. Lee, S. I. Kim and A. C. Evans: *NeuroImage* **27** (2005) 210–221.
 - 16) K. Okamoto and M. Fukuhara: *Int. J. Remote Sens.* **17** (1996) 1735–1749.
 - 17) Y. Kageyama and M. Nishida: *Electr. Eng. Jpn.* **148** (2004) 65–73.
 - 18) W. Oh and W. B. Lindquist: *IEEE Trans. Pattern Anal. Mach. Intell.* **21** (1999) 590–602.
 - 19) A. Kitamoto and M. Takagi: *Trans. IEICE* **J81-D-II** (1998a) 1160–1172 (in Japanese).
 - 20) A. Kitamoto and M. Takagi: *Trans. IEICE* **J81-D-II** (1998b) 2582–2597 (in Japanese).
 - 21) A. Kitamoto and M. Takagi: *Pattern Anal. Appl.* **2** (1999) 31–43.
 - 22) A. Kitamoto and M. Takagi: *Syst. Comp. Japan* **31** (2000) 57–76.
 - 23) P. K. Sahoo, S. Soltani, A. K. C. Wong and Y. C. Chen: *Comp. Vision Graph. Image Process.* **41** (1988) 233–260.
 - 24) N. R. Pal and S. K. Pal: *Pattern Recogn.* **26** (1993) 1277–1294.
 - 25) M. Sezgin and B. Sankur: *J. Electron. Imag.* **13** (2004) 146–168.
 - 26) P. C. Baveye *et al.*: *Geoderma* **157** (2010) 51–63.
 - 27) P. Iassonov, T. Gebrenegus and M. Tuller: *Water Resour. Res.* **45** (2009) W09415.
 - 28) A. Kitamoto: Technical Report of IEICE, PRMU99-166, (1999) pp. 7–14 (in Japanese).
 - 29) A. Kitamoto: Proc. Joint IAPR Int. Workshops SSPR 2000 and SPR 2000, Alicante, Spain, (Springer, Berlin/Heidelberg, 2000) pp. 521–531.
 - 30) I. Sekita, T. Kurita, N. Otsu and N. N. Abdelmalek: *Trans. IEICE* **J78-D-II** (1995) 1806–1812 (in Japanese).
 - 31) N. Otsu: *IEEE Trans. Syst. Man Cybernet.* **SMC-9** (1979) 62–66.
 - 32) T. Kurita, N. Otsu and N. Abdelmalek: *Pattern Recogn.* **25** (1992) 1231–1240.
 - 33) J. Kittler and J. Illingworth: *Pattern Recogn.* **19** (1986) 41–47.
 - 34) M. Kato, M. Takahashi and K. Kaneko: *Geoinformatics* **19** (2008) 132–133 (in Japanese).
 - 35) T.-W. Lo, K. B. Coyner and M. N. Toksoz: *Geophysics* **51** (1986) 164–171.
 - 36) J. Zhang, T.-f. Wong, T. Yanagidani and D. M. Davis: *Mech. Mater.* **9** (1990) 1–15.
 - 37) D. J. Hart and H. F. Wang: *J. Geophys. Res.* **100** (1995) 17741–17751.
 - 38) B. Menéndez, W. Zhu and T.-f. Wong: *J. Struct. Geology* **18** (1996) 1–16.
 - 39) J. M. Schembre and A. R. Kovscek: *J. Petroleum Sci. Eng.* **39** (2003) 159–174.
 - 40) M. Takahashi, M. Kato, Y. Urushimatsu and H. Park: *J. Japan Soc. Eng. Geology* **50** (2009) 280–288 (in Japanese).
 - 41) J. C. Jaeger, N. G. W. Cook and R. W. Zimmerman: *Fundamentals of Rock Mechanics*, 4th edn., (Blackwell, Malden, MA, 2007) p. 475.
 - 42) S. Kawasaki, A. Murao, N. Hiroyoshi, M. Tsunekawa and K. Kaneko: *J. Japan Soc. Eng. Geology* **47** (2006) 2–12 (in Japanese).
 - 43) H. M. Makhlof and J. J. Stewart: Proc. Int. Symp. on Wave Propagation and Dynamic Properties of Earth Materials, (University of New Mexico Press, Albuquerque, New Mexico, 1967) pp. 825–837.
 - 44) J. N. Kapur, P. K. Sahoo and A. K. C. Wong: *Comp. Vision Graph. Image Process.* **29** (1985) 273–285.
 - 45) H. Shoji: Graduation Thesis, (Hokkaido University, Sapporo, 2008) p. 82 (in Japanese).
 - 46) S. Ogata, S. Kawasaki, N. Hiroyoshi, M. Tsunekawa, K. Kaneko and R. Terajima: *Rock Engineering in Difficult Ground Conditions: Soft Rocks and Karst*, (EUROCK 2009, Dubrovnik, Cavtat, Croatia), ed. by I. Vrkljan, (Taylor & Francis Group, London, 2010) pp. 339–344.